J. Fluid Mech. (1998), *vol.* 368, *pp.* 339–357. Printed in the United Kingdom

Secondary instability of cross-flow vortices in Falkner–Skan–Cooke boundary layers

By MARKUS HÖGBERG[1] AND DAN HENNINGSON[1,2]

[1]Department of Mechanics, KTH, S-100 44, Stockholm, Sweden

[2]FFA, Box 11021, S-16111, Bromma, Sweden

(Received 18 June 1997 and in revised form 14 April 1998)

Linear eigenvalue calculations and spatial direct numerical simulations (DNS) of disturbance growth in Falkner–Skan–Cooke (FSC) boundary layers have been performed. The growth rates of the small-amplitude disturbances obtained from the DNS calculations show differences compared to linear local theory, i.e. non-parallel effects are present. With higher amplitude initial disturbances in the DNS calculations, saturated cross-flow vortices are obtained. In these vortices strong shear layers appear. When a small random disturbance is added to a saturated cross-flow vortex, a low-frequency mode is found located at the bottom shear layer of the cross-flow vortex and a high-frequency secondary instability is found at the upper shear layer of the cross-flow vortex. The growth rates of the secondary instabilities are found from detailed analysis of simulations of single-frequency disturbances. The low-frequency disturbance is amplified throughout the domain, but with a lower growth rate than the high-frequency disturbance, which is amplified only once the cross-flow vortices have started to saturate. The high-frequency disturbance has a growth rate that is considerably higher than the growth rates for the primary instabilities, and it is conjectured that the onset of the high-frequency instability is well correlated with the start of transition.

1. Introduction

A disturbance in an unstable laminar flow often results in transition to a turbulent state, but in some cases it takes the flow into another laminar more complicated state. If the disturbances are small, compared to the base flow, the analysis can be simplified by using linearized equations for the disturbance evolution. If the disturbances reach a higher level, nonlinear effects become important. Traditionally, transition prediction in two-dimensional flows has been based on the study of the evolution of so-called Tollmien–Schlichting (T–S) waves. The growth of these waves is governed by the Orr–Sommerfeld equation. For flows where this exponential instability is weak, recent work by Butler & Farrell (1992), Reddy & Henningson (1993) and Trefethen *et al.* (1993) has shown the importance of transiently growing three-dimensional disturbances. Typically, this growth results in streaky structures rather than two-dimensional waves. For an overview of results regarding transient growth, see Henningson (1995).

In three-dimensional boundary layer flows, there are additional processes that can lead to transition. Examples of such flows are flow over swept wings, rotating discs, cones and spheres and cones at an angle of attack. More about these flows can be found in Reed & Saric (1989). In a three-dimensional flow the direction of the base flow is a function of the normal coordinate, and the velocity profile usually

has an inflection point. This means that there usually exists an inviscid inflectional instability, see e.g. Gregory, Stuart & Walker (1955). This primary instability may result in amplification of oblique travelling waves and of stationary vortices. Local linear stability theory predicts non-stationary modes to be more amplified than stationary modes. However, in most experiments the stationary ones are preferred (Reed & Saric 1989). The reason may be that the effective receptivity of stationary cross-flow modes to surface roughness is stronger than that of travelling waves to free-stream fluctuations, see Choudhari (1994), Morkovin (1969, 1977) for receptivity issues. Another reason may be related to phase averaging in the experimental measuring techniques. Only recently have measurements been made where the travelling modes have been introduced in three-dimensional boundary layer flow in a repeatable manner, see e.g. Lingwood (1996), Lerche (1997).

Effects of transient growth have also been seen in three-dimensional boundary layers, see Breuer & Kuraishi (1994), although it may here be of less importance due to the large growth rates of the primary exponential instabilities present.

In addition to the convective instabilities discussed so far, there is evidence that three-dimensional boundary layers may experience so-called absolute instabilities. These are instabilities which grow at a fixed location, without being swept downstream by the base flow. In a rotating disc boundary layer a true absolute instability has been found by Lingwood (1995), whereas for infinite swept plate boundary layers a chordwise absolute instability has been found, see Lingwood (1997). The disturbances associated with the latter absolute instability are still swept away in the spanwise direction and it is not clear that they would have any greater chance of causing transition than traditional convective instabilities.

When stationary cross-flow modes are initiated they grow according to linear theory until nonlinear effects cause saturation, and strong so-called cross-flow vortices develop. There are two types of secondary instability of stationary cross-flow vortices that have been observed in simulations and experiments by Kohama, Saric & Hoos (1991), Malik, Li & Chang (1994), Deyhle & Bippes (1996) and reported in a thesis of Lerche (1997): one low-frequency and one high-frequency instability. The low-frequency oscillations appear earlier in the breakdown process than the high-frequency one. The high-frequency oscillations have been detected just prior to breakdown. At this point, the strong cross-flow vortices contain sharp shear layers that appear to be inflectionally unstable, see Malik *et al.* (1994).

A slightly different scenario found by e.g. Müller & Bippes (1988), is that it was the travelling modes which dominated the transition process. The reason this occurred is the higher level of free-stream turbulence that was present in their experiment, which caused a stronger forcing of time-dependent disturbances. Although the amplitude of the stationary modes was smaller in this scenario, compared to flows with lower free-stream turbulence, the transition occurred earlier.

In this investigation we use direct numerical simulations (DNS) to obtain a physical understanding of the breakdown process of stationary cross-flow vortices. Direct numerical simulations have been used previously to study the stability and transition associated with cross-flow vortices, e.g. Müller, Bestek & Fasel (1993), Spalart, Crouch & Ng (1994) and Wintergerste & Kleiser (1996). However, none have concentrated on the secondary instability of cross-flow vortices, which is the main aim of the present investigation. In a computational environment it is straightforward to generate a base flow including strong cross-flow vortices, and then add a desired disturbance. We use a base flow from an experiment made at DLR, Göttingen by Bippes (1991), that is suitable for investigations of cross-flow vortices and their stability features. Linear

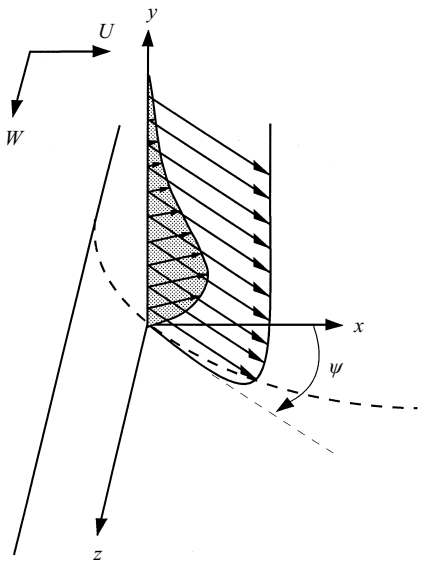

FIGURE 1. Coordinate system used in this report. ψ is the angle to the streamline of the flow in the free stream, U is the chordwise component and W is the spanwise component. The dotted line is the streamline of the flow in the free stream over a flat plate with a pressure gradient in the x-direction.

stability calculations are made as well as DNS, and the results are analysed and compared. In addition results on secondary instability of cross-flow vortices are also reported.

2. Background

2.1. *Falkner–Skan–Cooke profiles*

We consider an infinite swept flat plate where $\partial/\partial z = 0$. For this case the dimensional boundary layer equations according to Schlichting (1979) become

$$u^*\frac{\partial u^*}{\partial x^*} + v^*\frac{\partial w^*}{\partial y^*} = U_\infty^*\frac{\mathrm{d}U_\infty^*}{\mathrm{d}x^*} + \nu\frac{\partial^2 u^*}{\partial y^{*2}}, \tag{2.1}$$

$$u^*\frac{\partial w^*}{\partial x^*} + v^*\frac{\partial w^*}{\partial y^*} = \nu\frac{\partial^2 w^*}{\partial y^{*2}}, \tag{2.2}$$

$$\frac{\partial u^*}{\partial x^*} + \frac{\partial v^*}{\partial y^*} = 0, \tag{2.3}$$

with the boundary conditions

$$u^* = v^* = w^* = 0 \quad \text{at} \quad y^* = 0, \tag{2.4}$$

$$u^* \to U_\infty^*, \quad w^* \to W_\infty^* \quad \text{as} \quad y^* \to \infty, \tag{2.5}$$

where u^*, v^*, w^* are the chordwise (x), normal (y) and spanwise (z) velocity components, respectively, and * denotes dimensional quantities. See figure 1 for a definition of the coordinate system. We assume that the chordwise base flow at the boundary layer edge obeys a power law according to $U_\infty^* = U_0^*(x^*/x_0^*)^m$ and that $W_\infty^* =$ constant.

A self-similar solution may be found if we select

$$\eta = \{(m+1)U_\infty^*/2\nu x^*\}^{1/2} y^*. \tag{2.6}$$

Introducing the stream function

$$\Psi^* = (2U^*\nu x^*/m+1)^{1/2} f(\eta) \tag{2.7}$$

with $u^* = \partial\Psi^*/\partial y^*$ and $v^* = -\partial\Psi^*/\partial x^*$ and $w^* = W_\infty^* g(\eta)$ reduces the boundary layer equations to a function of the single variable η, and we have

$$f''' + ff'' + \beta_H(1 - f'^2) = 0, \tag{2.8}$$

$$g'' + fg' = 0, \tag{2.9}$$

where the Hartree parameter is $\beta_H = 2m/(m+1)$ and the boundary conditions are

$$f = f' = g = 0 \quad \text{if} \quad \eta = 0, \tag{2.10}$$

$$f' \to 1, \quad g \to 1 \quad \text{as} \quad \eta \to \infty; \tag{2.11}$$

f' and g can then be combined into the Falkner–Skan–Cooke velocity profiles, see Cooke (1950), as

$$U(y) = f'[\eta(y)], \tag{2.12}$$

$$W(y) = \frac{W_\infty^*}{U_\infty^*} g[\eta(y)], \tag{2.13}$$

with $y = y^*/\delta_0^*$. Note that

$$\delta^* = \{(m+1)U_\infty^*/2\nu x^*\}^{-1/2} \int_0^\infty (1 - f')\mathrm{d}\eta \tag{2.14}$$

which implies that

$$\delta_0^* = \{(m+1)U_0^*/2\nu x_0^*\}^{-1/2} C \tag{2.15}$$

where

$$C = \int_0^\infty (1 - f')\mathrm{d}\eta. \tag{2.16}$$

Then we have

$$\eta = C \left\{ \frac{U_\infty^* x_0^*}{U_0^* x^*} \right\}^{1/2} y, \tag{2.17}$$

where x_0^* is a fixed position. The profiles (2.12) and (2.13) will be used as a base flow in the stability investigations and as initial conditions in the direct numerical simulations presented.

2.2. *Linear theory*

The most common way of investigating the stability of a flow to small disturbances is to assume that the flow can be divided into two parts,

$$(u, v, w) = (U, 0, W) + (u', v', w') \tag{2.18}$$

where U and W are the base flow components in the chordwise and spanwise directions, respectively. It is here assumed that the parallel flow assumption holds, i.e. the base flow components only vary with the normal coordinate. The primed quantities represent a small perturbation. We also assume wave-like disturbance of the form

$$u' = \hat{u}\mathrm{e}^{\mathrm{i}(\alpha x + \beta z - \omega t)}, \tag{2.19}$$

where α and β are the x- and z-components of the wavenumber vector and ω is the frequency and $\hat{u}$ is the complex amplitude function for the chordwise velocity. Inserting these assumptions into the Navier–Stokes equations and linearizing, we find the resulting disturbance equations that can be reduced to the following set of two coupled equations:

$$[\mathrm{D}^2-(\alpha^2+\beta^2)]^2\hat{v}=\mathrm{i}R[(\alpha U+\beta W-\omega)[\mathrm{D}^2-(\alpha^2+\beta^2)]-(\alpha\mathrm{D}^2U+\beta\mathrm{D}^2W)]\hat{v}, \quad (2.20)$$

$$(\alpha\mathrm{D}W-\beta\mathrm{D}U)\hat{v}=\left[\frac{1}{R}(\mathrm{D}^2-(\alpha^2+\beta^2))-\mathrm{i}(\alpha U+\beta W-\omega)\right]\hat{\eta}, \quad (2.21)$$

where $\hat{v}$ and $\hat{\eta}=\mathrm{i}(\beta\hat{u}-\alpha\hat{w})$ are the amplitude functions for the normal velocity and the normal vorticity, respectively. D stands for the differential operator in the wall-normal direction. The boundary conditions are

$$\hat{v}(0)=0, \quad \mathrm{D}\hat{v}(0)=0, \quad \hat{\eta}(0)=0, \quad (2.22)$$

$$\hat{v}(y)\to 0, \quad \mathrm{D}\hat{v}(y)\to 0, \quad \hat{\eta}(y)\to 0 \quad \text{as} \quad y\to\infty. \quad (2.23)$$

Here R is the Reynolds number based on the velocity scale U_∞ and the displacement thickness δ^*, both taken at the streamwise location x_0.

Equation (2.20) is referred to as the Orr–Sommerfeld equation, and (2.21) is known as the Squire equation. The base flow used in this investigation is found from the Falkner–Skan–Cooke (FSC) velocity profiles given in the previous subsection. The equations, considered as a spatial eigenvalue problem, are solved using a spectral collocation technique with Chebyshev polynomials in the normal direction, and a companion matrix technique. The technique is explained e.g. in Lundbladh *et al.* (1994).

Results from the spatial eigenvalue problem will be compared to results from the parabolic stability equations (PSE). This extended approximation offers an effective way to take non-parallel effects into account using an advanced multiple scales technique, first developed by Bertolotti, Herbert & Spalart (1992). In this paper we present results by A. Hanifi (private communication) as a check on the direct numerical simulation results. The PSE code used is described in Hanifi *et al.* (1994).

2.3. *Description of the laminar base flow*

The computations model an experiment made by Bippes (1991) at DLR in Göttingen, where the flow over a swept flat plate was designed to approximate FSC flow. In the experiment small discs were placed periodically close to the front of the plate, in order to excite well-defined cross-flow vortices. Their spanwise spacing was chosen to be approximately the same as that of the fastest growing stationary cross-flow disturbance. We will use the flow conditions of this experiment as the laminar base flow in the present investigation.

It is important to note that we are not primarily concerned with the details of the numerical modelling of the experiment. For us it suffices to know that we have chosen a test case which is of practical interest and can be realized in an experiment. In addition, the previous investigations of Bippes (1991) did not address the secondary instability of the cross-flow vortices, which are the emphasis of the present paper, but rather their interaction with travelling waves. Unfortunately, the later work dealing with the high-frequency secondary instability by Lerche (1997), a student of Hans Bippes, was done at slightly different flow conditions. Thus a detailed quantitative comparison of the present results with that of Lerche (1997) cannot be made, and we have to be content to compare the qualitative features.

x	R_{δ^*}	ψ (deg.)
0	337.9	55.3
20.59	351.2	54.7
209.5	461.6	50.9
220.0	467.3	50.7
261.9	490.0	50.0
500.0	694.1	44.98

TABLE 1. Relations between different parameters at different locations on the flat plate. R_{δ^*} is the Reynolds number based on the displacement thickness and the local free-stream velocity and ψ is the angle of the external streamline.

In all of the simulations presented here the inflow position in the computational domain will be at $x = 0$, corresponding to a Reynolds number of $R = 337.9$. Unless otherwise stated, the calculations presented will be scaled with the displacement thickness and the free-stream velocity at this position. With this scaling the distance from the leading edge to the start of the computational box can be found using equation (2.15) and is

$$x_0 = \frac{m+1}{2C^2}R = 354.0, \tag{2.24}$$

and the distance between the small discs generating the cross-flow vortices is about 25.14, corresponding to a spanwise wavenumber of about ± 0.25. The outflow position in the computations is located 500 initial displacement thicknesses downstream, which corresponds to $R_{\delta^*} = 694.1$. Note that when R_{δ^*} rather than R is used, we assume that the Reynolds number is based on the local displacement thickness and free-stream velocity. The base velocity at the boundary layer edge in the experiment by Bippes (1991) can now be written:

$$U_\infty = \left(\frac{x}{x_0} + 1\right)^{0.34207}, \tag{2.25}$$

$$W_\infty = 1.442. \tag{2.26}$$

See Högberg & Henningson (1996) for a further discussion of issues relating to the computational modelling of the experiment and table 1 for the relationships between the coordinates used in the computational box, the Reynolds number and the angle of the external streamline of the FSC flow.

2.4. *Linear stability characteristics of the base flow*

In figure 2(a, b) the behaviour of the unstable modes with a wavenumber $\beta = -0.25$ is shown at a chordwise position $x = 261.9$, corresponding to $R_{\delta^*} = 490.0$. This chordwise position is about halfway between the inflow and the outflow of the computational domain used in the numerical simulations, and should thus give a good idea of the typical behaviour of the unstable modes expected in the calculations. The results are found by use of the Orr–Sommerfeld and Squire equations derived in § 2.2.

Figure 2(a) shows the growth rate vs. the frequency, and it is clear that travelling modes are more unstable than the stationary one. In figure 2(b) the growth rates of the stationary mode and the travelling mode with largest growth rate ($\omega = -0.048\,35$) are shown vs. the angle of the wavenumber vector. It is seen that the travelling modes are unstable for a broad range of angles, whereas the stationary mode is only unstable

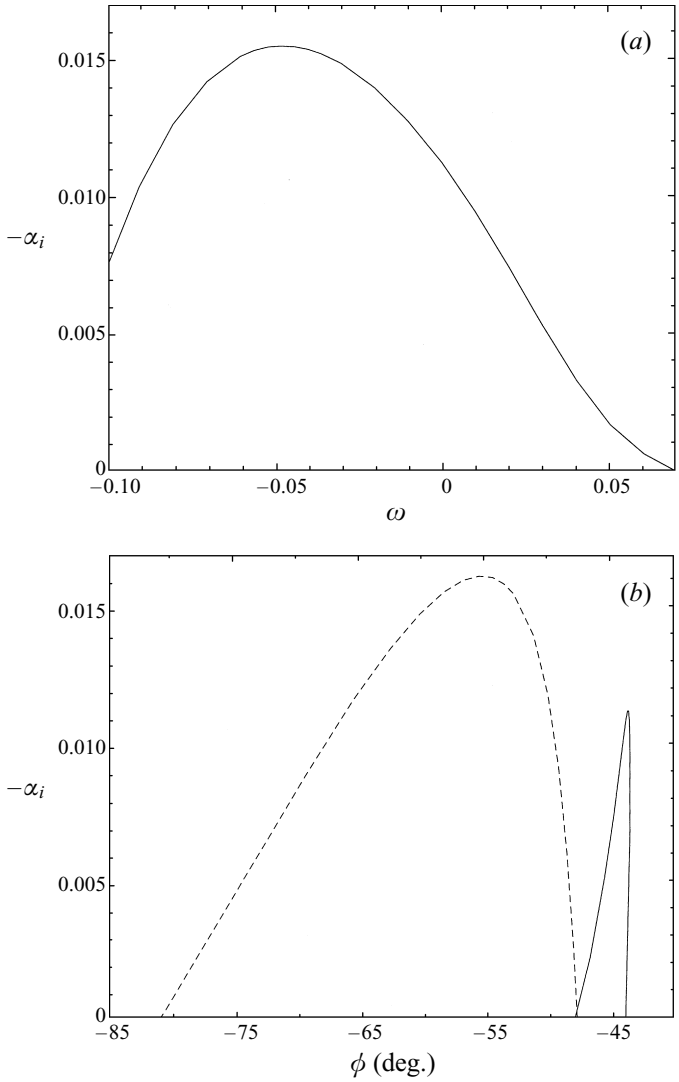

FIGURE 2. Growth rates for $\beta = 0.25$ at $x = 261.9$. (*a*) Growth rate vs. frequency. (*b*) Growth rate vs. angle of wavenumber vector. Solid line: $\omega = 0$; dashed: $\omega = -0.04835$.

for waves with a wave angle of about 45°. This implies that the phase lines of the unstable stationary modes, and thus the direction of the resulting cross-flow vortices are about 45°. This angle is close to the angle of the FSC free-stream velocity vector at that chordwise position.

2.5. *Direct numerical simulations*

The incompressible Navier–Stokes equations, for flow over a flat plate, are discretized using a spectral method. For spatial simulations, a fringe region technique is used to allow a streamwise inflow and outflow of the computational domain, retaining the periodic boundary conditions. At a constant distance from the flat plate an artificial boundary is introduced and a free-stream boundary condition applied. The horizontal directions are discretized using Fourier series and the normal direction

using Chebyshev series. Time integration is performed using a third-order Runge–Kutta method for the advective and forcing terms and a Crank–Nicolson method for the viscous terms. More about the code can be found in Lundbladh, Henningson & Johansson (1992) and Lundbladh *et al.* (1994). The disturbances in the flow field are generated using localized volume forces,

$$\frac{\partial \boldsymbol{u}}{\partial t} = NS(\boldsymbol{u}) + \lambda(x)(\boldsymbol{u} - \boldsymbol{u}_\lambda) + \boldsymbol{F}, \tag{2.27}$$

where $\boldsymbol{u} = (u, v, w)$. The term $\lambda(x)(\boldsymbol{u} - \boldsymbol{u}_\lambda)$ is the fringe forcing, where $\boldsymbol{u}_\lambda$ is the desired flow solution in the fringe and $\lambda(x)$ is a non-negative fringe function which is non-zero only in the fringe region. The localized disturbance forcing is given by the vector $\boldsymbol{F} = (F_1, F_2, F_3)$. It is possible to generate different kinds of disturbances, both random and harmonic.

The random forcing is constructed by randomly distributing the amplitude among a given number of spanwise Fourier components at each time interval. The random forcing, which is directed normal to the wall, has the form

$$F_2 = F_{rand} = \mathrm{e}^{(-((x-x_0)/x_{scale})^2-(y/y_{scale})^2)} f(z,t), \tag{2.28}$$

where

$$f(z,t) = t_{amps} g(z) + t_{ampt}[(1 - b(t))h^i(z) + b(t)h^{i+1}(z)] \tag{2.29}$$

and

$$i = \mathrm{int}(t/t_{dt}), \tag{2.30}$$

$$b(t) = 3p^2 - 2p^3, \tag{2.31}$$

$$p = t/t_{dt} - i, \tag{2.32}$$

$g(z)$ and $h^i(z)$ are Fourier series of unit amplitude with random coefficients, and t_{ampt}, t_{amps} are the time-dependent and the stationary disturbance amplitude, respectively. The number of random coefficients in each Fourier series is given by a parameter named n_{modes}. Random values are generated for $h^i(z)$ with the spacing t_{dt} in time and then the ramp function $b(t)$ is used to interpolate this to a smooth forcing. The frequency spectrum for the random part of the forcing is almost constant in the range $\omega = 0$ to $\omega = 1/t_{dt}$ and then decays quickly to zero outside, see figure 3.

The harmonic disturbance is constructed as an exponentially decaying function centred at $y = 0$ and $x = x_{loc0}$. It is also possible to give a relationship between the x- and z-component of the disturbance to align the disturbance to a streamline. The harmonic forcing has the form

$$F_2 = F_{harm} = \mathrm{amp}_y \mathrm{e}^{(-(y/y_{scale})^2)} g(x,z) f(t) h_1(t), \tag{2.33}$$

where

$$g(x,z) = \cos(2\pi(z - x l_{skew})/z_{scale}) \mathrm{e}^{-[(x-x_{loc0})/x_{scale}]^2} \tag{2.34}$$

and

$$f(t) = S(-t/t_{scale}), \tag{2.35}$$

where

$$S(x) = \begin{cases} 0, & x \leqslant 0 \\ 1/\left[1 + \exp\left(\dfrac{1}{x-1} + \dfrac{1}{x}\right)\right], & 0 < x < 1 \\ 1, & x \geqslant 1 \end{cases}$$

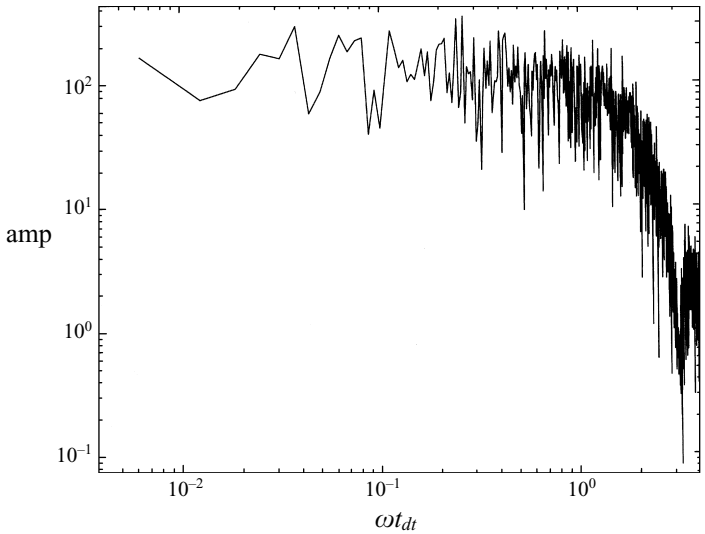

FIGURE 3. Frequency spectrum for the random part of the local forcing.

and

$$h_1(t) = \cos(\omega_h t). \tag{2.36}$$

The function $f(t)$ must be used to give a smooth turn-on of the forcing to avoid problems with transients that may grow and cause transition in the flow. For stationary disturbances ω_h is chosen as zero, otherwise it is the ω given in table 2. In the simulations presented in this paper amp_y is designated t_{amps} for stationary disturbances or t_{ampt} for time-dependent (oscillating) disturbances.

Table 2 contains information about the different flow cases that have been simulated. Cases 1–4 have small enough amplitudes such that the disturbance evolution is linear, with the latter two simulations having a computational box width ten times the former and a random disturbance generation. Cases 5–11 all have the smaller spanwise box size and have disturbances for which nonlinear effects are significant. The resolution has been checked in several ways. Comparing the results from cases 5 and 6, 8 and 9, and 7 and 10 confirmed that the resolution is sufficient in our simulations. The growth rate curves from cases 5 and 6 were the same, and so were they for cases 8 and 9.

3. Results

3.1. *Comparison between linear theory and DNS*

As a check on the numerics we start with a comparison between results of linear stability theory, PSE and direct numerical simulations. We consider the exponential amplification of disturbances in a spatially growing boundary layer. First a start field is generated, using the FSC profiles, and then a stationary or time-dependent disturbance is generated using a volume force at $x = 20.95, R_{\delta^*} = 351.2$ see table 2, to obtain the cross-flow vortices or the travelling waves. The Navier–Stokes equations are then solved until a stationary or periodic state is achieved.

First, we will verify that the spanwise spacing of the disturbance generators in the experiments corresponds to a mode of maximum growth rate. We use a computational

			Stationary forcing			Time-dependent forcing			
Case	Box	Resolution	Pos.	Type	t_{amps}	Pos.	Type	t_{ampt}	ω
1	A	$384 \times 49 \times 4$	20.59	A	10^{-5}				
2	A	$384 \times 49 \times 4$				20.59	C	5×10^{-6}	0.04835
3	B	$192 \times 49 \times 48$	20.59	B	10^{-3}				
4	B	$192 \times 49 \times 48$				20.59	D	10^{-3}	
5	A	$384 \times 49 \times 16$	20.59	A	3.6×10^{-3}				
6	A	$576 \times 65 \times 24$	20.59	A	3.6×10^{-3}				
7	A	$576 \times 49 \times 24$	20.59	A	3.6×10^{-3}	20.59	D	10^{-5}	
8	A	$576 \times 65 \times 24$	20.59	A	3.6×10^{-3}	209.5	D	10^{-4}	
9	A	$768 \times 65 \times 24$	20.59	A	3.6×10^{-3}	209.5	D	10^{-4}	
10	A	$768 \times 65 \times 24$	20.59	A	3.6×10^{-3}	20.59	C	10^{-6}	0.0957
11	A	$768 \times 65 \times 24$	20.59	A	3.6×10^{-3}	220.0	C	10^{-3}	0.957

Forcing	Type
A	Stationary-local, $x_{scale} = 10$, $y_{scale} = 1$, $z_{scale} = -25.14$ $l_{skew} = 1$, $t_{scale} = -400$
B	Stationary-trip, $x_{scale} = 6$, $y_{scale} = 1$, $n_{modes} = 45$
C	Harmonic-local, $x_{scale} = 10$, $y_{scale} = 1$, $z_{scale} = -25.14$ $l_{skew} = 1$, $t_{scale} = -400$
D	Random-trip, $x_{scale} = 10$, $y_{scale} = 1$, $n_{modes} = 9$, $t_{dt} = 1$.

TABLE 2. Summary of the different simulations where Box A denotes $500 \times 8 \times 25.14$ and Box B denotes $500 \times 8 \times 251.4$. Lower table shows the type of forcing.

domain in the spanwise direction which is ten times greater than that associated with a single mode and introduce random stationary disturbances along a line parallel to the leading edge. In figure 4, which is labelled as case 3 in table 2, the normal velocity associated with the cross-flow eigenmode is shown viewed from below. The disturbances grow downstream and appear to be inclined at about 45°. This corresponds to the most unstable direction in figure 2(*b*) for the zero-frequency disturbance. At the end of the box in figure 4 there are ten vortices, corresponding to a wavelength in the z-direction that is equivalent to the width of the computational box used in the rest of the direct numerical simulations presented. Thus, the spacing of the roughness elements used in the experiments by Bippes (1991) to generate the vortices is indeed close to the wavelength of the most unstable zero-frequency mode. In case 4, a small-amplitude random disturbance was introduced at the same location as in case 3. This disturbance gave oblique, unsteady, travelling waves similar to what Müller & Bippes (1988) found in a study with higher free-stream forcing. In their case the transition process was dominated by the travelling modes.

The growth rate is the complex part of the chordwise wavenumber, $-\alpha_i$. In figure 5 this is compared to the chordwise derivative of the disturbance magnitude and results from cases 1, 2, 6 shown. Here the disturbance is generated with a stationary or time-dependent (harmonic) forcing. Note that due to the presence of non-parellel effects the correspondence is poor between linear theory and DNS. This is also true for the non-stationary disturbance which is chosen to correspond to the one with

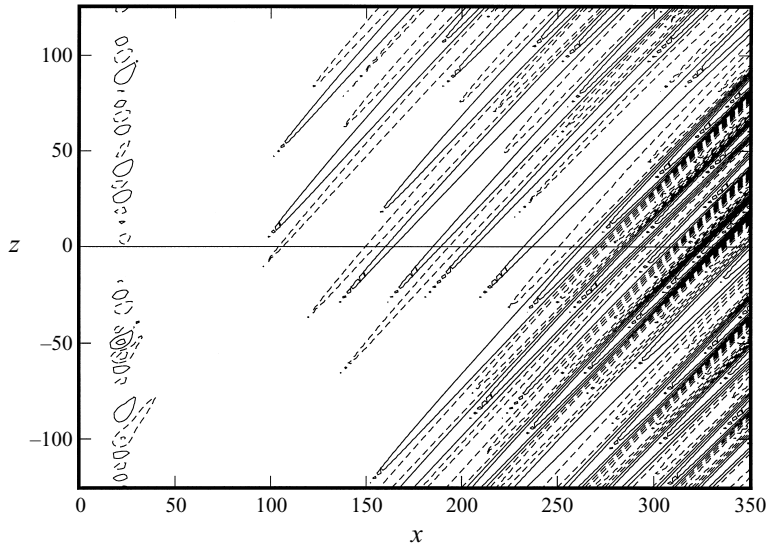

FIGURE 4. Contour lines of the disturbance velocity in the normal direction at $y = 0.5$. The spacing between the contours is 0.000 05. The vortices are generated by random stationary disturbances at $x = 20.95$.

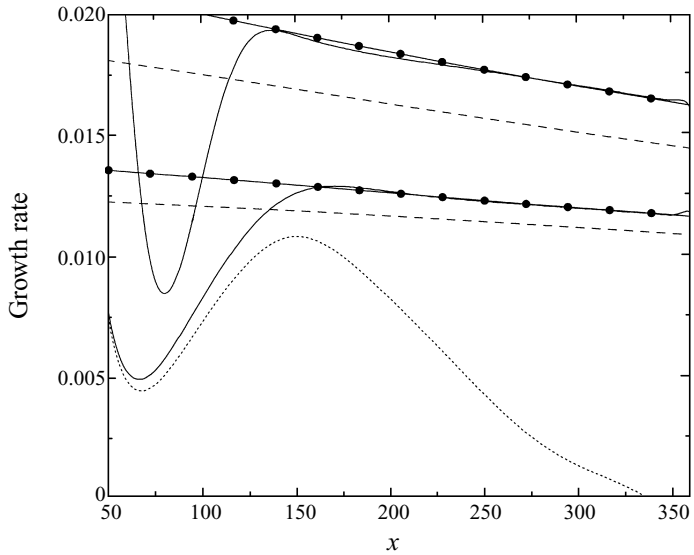

FIGURE 5. Growth rates vs. x. Solid lines: results from DNS calculations $\omega = 0$ (lower) and $\omega = -0.048\,35$ (upper); dashed: results of local eigenvalue computation for the same frequencies; dotted: DNS calculation for flow with saturated cross-flow vortices; filled circle: results from non-local PSE calculations (A. Hanifi, private communication).

maximum spatial growth rate. The good agreement between PSE results and DNS is a verification of the validity of the DNS results. The dips in the growth rate curves obtained from the DNS results from the fact that the local forcing does not input pure eigenmodes.

3.2. *Base flow – saturated vortices*

When the amplitude of the initial disturbance in the DNS is increased, the cross-flow vortices reach a saturated state, where the exponential disturbance growth is suppressed by nonlinear effects. For the flow with saturated vortices we have to increase the number of spectral modes as has been done in cases 5 and 6. The saturation can be seen in the decrease of the spatial growth rate of the stationary higher amplitude disturbance, also shown in figure 5. Contours of the chordwise velocity in an (x, y) plane are shown in figure 6(a), where the strong saturated vortices can be clearly seen.

As a starting point of the investigations of the interaction between travelling and stationary cross-flow modes a base flow with saturated cross-flow vortices can be used. To this base flow it is possible to add disturbances at different locations and with different structures. The saturated vortices contain strong shear layers, as seen in figure 6(a), which can be expected to support secondary instabilities. The shear layer at the bottom of the vortex is a result of fluid moving at a high velocity coming down with the vortex towards the wall into a region with a lower velocity. The layer on the side and at the top of the vortex is the result of low-velocity fluid being carried by the vortex into a region with fluid moving at a higher velocity.

3.3. *Secondary instabilities*

Figure 6(b, c) shows the response of the vortex to time-dependent random forcing at two different positions. These results will be described in some detail in the next two subsections.

3.3.1. *Low-frequency mode*

When a random time-dependent disturbance is located at the same x value as the stationary disturbance, a low-frequency oscillation develops downstream in the box. In figure 6(b) the r.m.s. values of the flow in the vortices are shown. It seems that the disturbance growth is supported mainly in the shear layer at the bottom of the vortex.

Figure 7 shows the instantaneous chordwise disturbance velocity in a field where the stationary time-averaged mean flow, u_{mean}, is subtracted. The levels of the disturbance are low compared to the vortex. In the frequency spectrum from case 7 in figure 8, taken in the centre of one of the vortex r.m.s. contours ($x = 337$, $y = 2.5$ and $z = 0$), there is a peak at a frequency in the region of the most amplified travelling wave. If we study figure 2(a), we can see that this frequency is unstable from linear analysis, but has a lower growth rate than it has in figure 13. If this frequency only is superimposed on the vortex, which is done in the simulations in case 10, we essentially reproduce figures 6(c) and 7. However, by integrating the solution long enough in time we can obtain a periodic solution and easily calculate its growth rate. The growth rate of this low-frequency mode is compared to the primary instabilities in figure 13. It is clear that the low-frequency mode grows faster than the primary ones if the vortices are strong. To obtain the growth rate for the low-frequency mode smoothing was used on the original data.

These results indicate that the low-frequency mode can be viewed as an interaction between the zero-frequency and amplified travelling modes, since the presence of vortices modifies an already existing primary instability into what Fischer & Dallmann (1991) calls a secondary instability. The main changes in the primary travelling mode due to the presence of the finite-amplitude cross-flow vortex are the increased growth

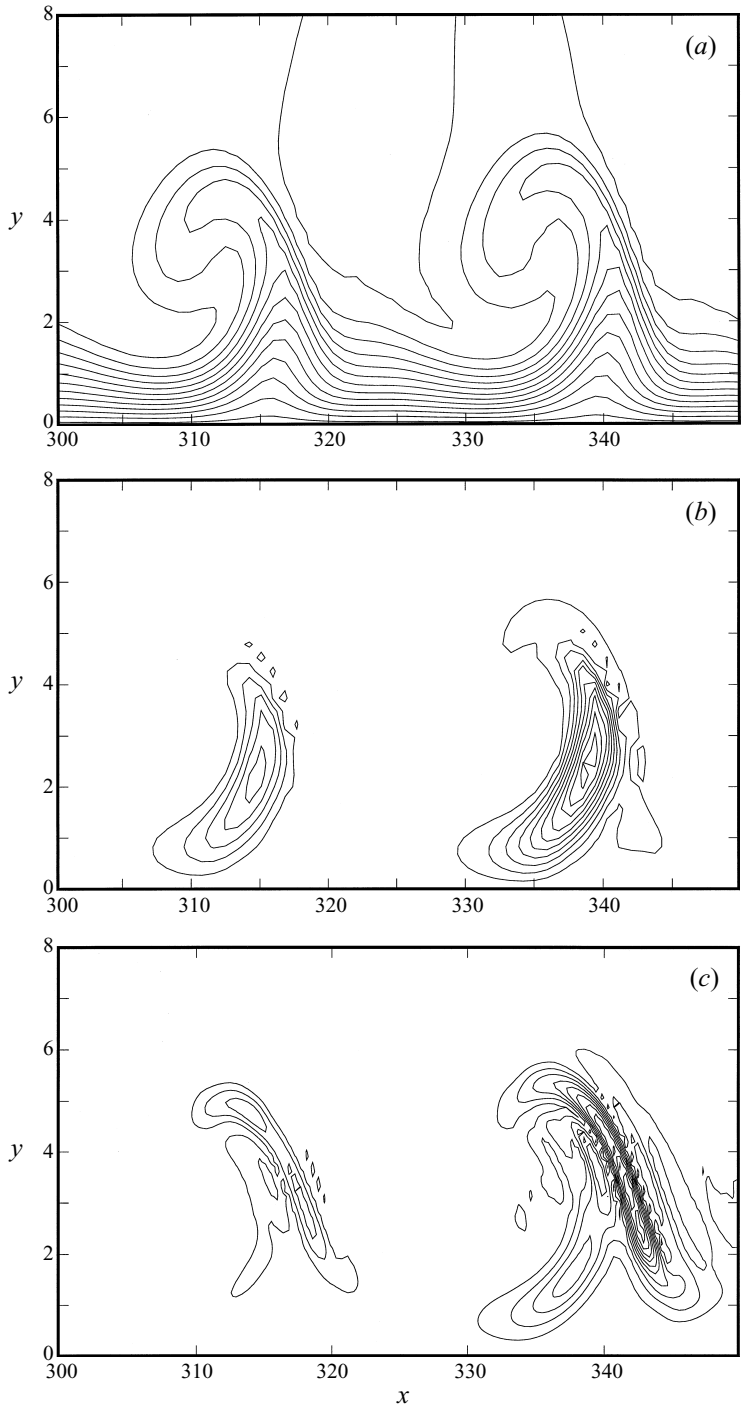

FIGURE 6. Cross-flow vortices generated at $x = 20.95$ and their secondary instability. (*a*) Contours of chordwise velocity at $z = 0$. Contour spacing 0.1. (*b*) Contours of r.m.s. of u at $z = 0$, with contour spacing 0.0002; non-stationary random-frequency disturbance generated at $x = 20.95$. (*c*) Contours of r.m.s. of u at $z = 0$, with contour spacing 0.001; non-stationary random-frequency disturbance generated at $x = 209.5$.

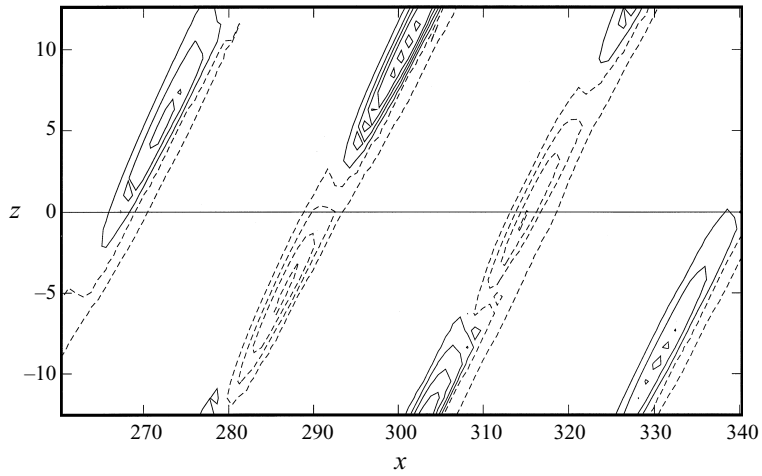

FIGURE 7. Contours of $u - u_{mean}$ at $y = 3$, spacing 0.0002.

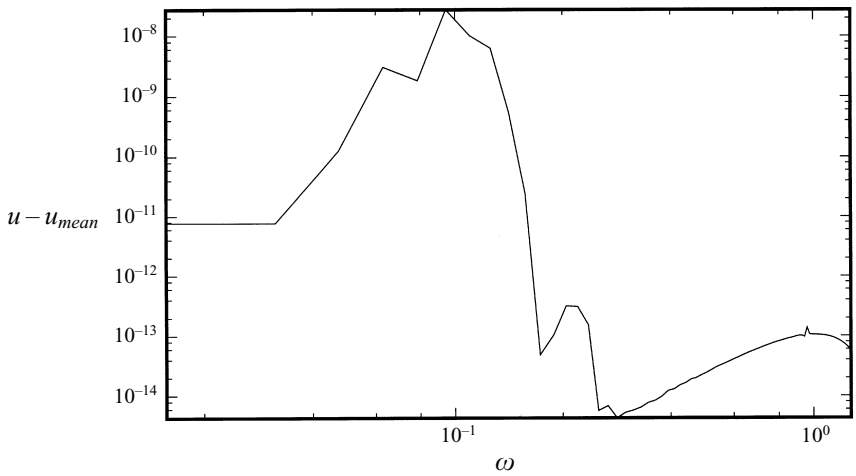

FIGURE 8. Frequency spectrum at $x = 337$, $y = 2.5$ and $z = 0$, which is located at the point where the maximum r.m.s. of the disturbance occurs.

rate and the modification of the eigenfunction to have a local maximum at the lower shear layer of the stationary vortex.

3.3.2. *High-frequency secondary instability*

In experiments by Kohama *et al.* (1991) and Deyhle & Bippes (1996), a high-frequency instability has been observed just prior to transition. The frequency of this instability has been found to be about one order of magnitude higher than that of the most amplified travelling wave, as was also found in calculations by Malik *et al.* (1994).

To trigger this instability in our base flow the random disturbance generation was moved downstream to a position where the vortex was close to saturation. The most unstable frequencies supported by the saturated vortex were found by adding a random disturbance to the base flow at $x = 209.5$. This disturbance triggered both low- and high-frequency instabilities. See figure 6(*c*) for contours of the r.m.s. of the

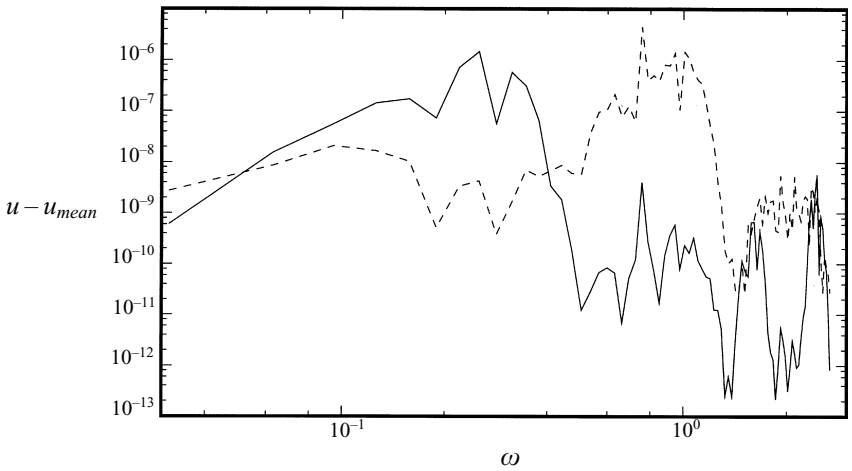

FIGURE 9. Solid: Frequency spectrum at $x = 335$, $y = 1.0$, $z = 0$; dashed: at $x = 337$, $y = 5.2$, $z = 0$ for cross-flow vortex with random frequency disturbance at $x = 209.5$.

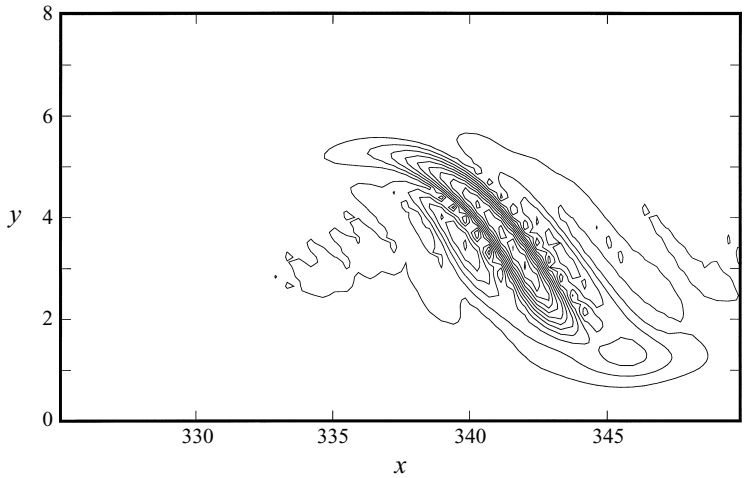

FIGURE 10. Cross-flow vortices generated by a stationary disturbance at $x = 20.59$. R.m.s. of u, with contour spacing 0.00025 non-stationary harmonic high-frequency disturbance generated at $x = 220$.

chordwise velocity. If this is compared to figure 6(b) it is apparent that the extent of the r.m.s.-fluctuations increases when the random disturbance generator is moved downstream, particularly towards the top of the vortex. The frequency spectra in figure 9 show a peak both for a high and for a low frequency at different locations in the cross-flow vortex. The high frequency is found in the upper part of the vortex and the low frequency at the bottom.

From analysis of the frequency spectra it was found that a frequency of about $\omega = 0.957$ was the most unstable in the upper part of the vortex. In the calculations labelled case 10, a small-amplitude harmonic oscillation at this frequency was introduced centred at $x = 220$. A smooth turn-on of the forcing was used to avoid big transients that could lead to a transition in the flow. This disturbance grew mainly in the upper shear layer of the cross-flow vortex, see figure 10. In the thesis by Lerche (1997) the

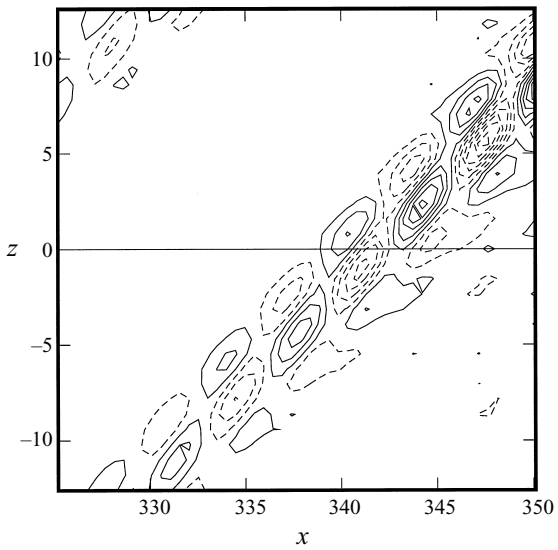

FIGURE 11. Contours of $u - u_{mean}$ at $y = 3$, spacing $= 0.000\,05$.

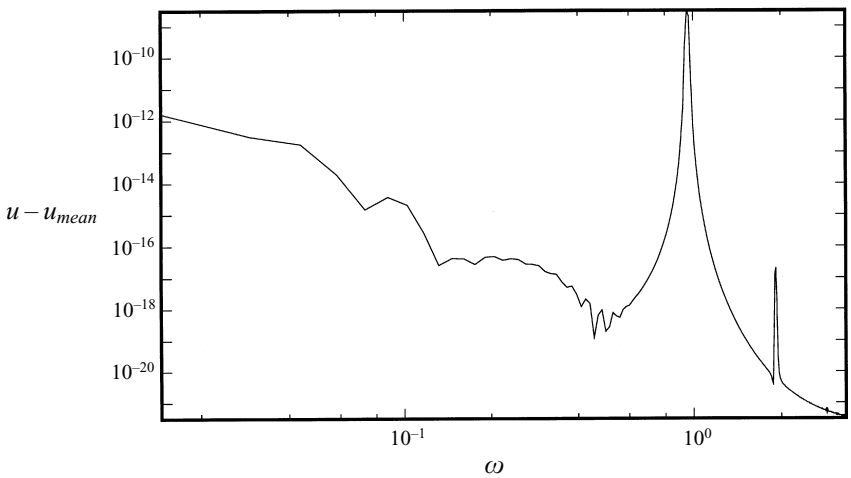

FIGURE 12. Frequency spectrum at $x = 342$, $y = 3.0$, $z = 0$ for cross-flow vortex with random frequency disturbance.

location of growing high-frequency disturbances is also found to be in the upper shear layer of the vortex.

Viewed from below in figure 11, where the time-averaged flow is subtracted, it is evident that the high-frequency oscillation is superimposed on the vortex. Note that the wavelength of the disturbance is about one quarter of that corresponding to the low-frequency secondary instability seen in figure 7.

The frequency spectrum in figure 12 shows a clean peak at the frequency of the generated disturbance. This is clearly a frequency that is highly amplified by the vortex.

The growth rate for this frequency is considerably higher than the growth rates of the primary instabilities, see figure 13. It is also higher than the growth rate of

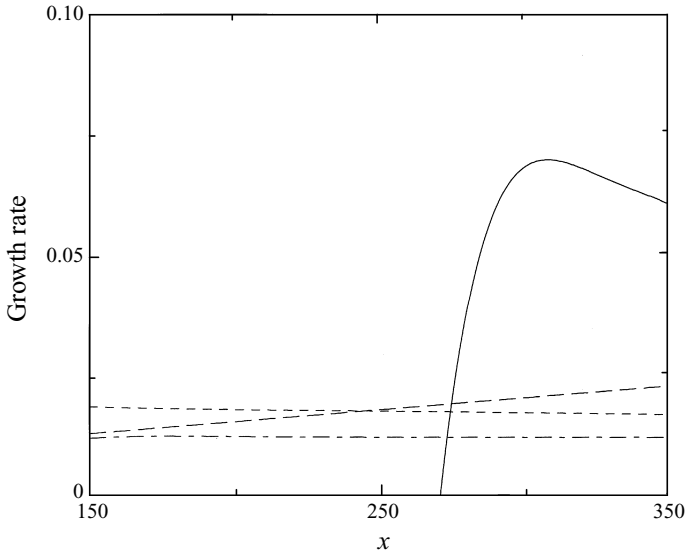

FIGURE 13. Growth rates for the secondary instabilities. Dash-dotted line: zero-frequency disturbance, short dashed: most unstable mode, long dashed: low-frequency mode, solid: high-frequency secondary instability.

the low-frequency mode. This indicates that the high-frequency secondary instability, when the conditions are favourable, dominates the transition process making it very rapid. One interesting aspect of the high-frequency instability is that the neutral point is located quite far downstream ($x = 270$). At that point the cross-flow vortex is almost saturated and the corresponding growth rate is close to zero, see figure 5. Note that to obtain the growth rate of the high-frequency secondary instability smoothing was used on the original data.

4. Summary and discussion

Linear eigenvalue calculations and direct numerical simulations of the evolution of disturbances in Falkner–Skan–Cooke boundary layers have shown that non-parallel effects on growth rates are present. This has been confirmed using non-parallel calculations based on the parabolic stability equations. The non-parallel effects are larger for travelling waves than for stationary disturbances.

When stationary disturbances with higher amplitudes are introduced in the direct numerical simulations, saturated cross-flow vortices are obtained. The secondary instability of these vortices is considered by superimposing small random disturbances on the cross-flow vortices. A low-frequency mode is found located at the bottom shear layer of the cross-flow vortex, and a high-frequency secondary instability is found at the upper shear layer of the cross-flow vortex. In agreement with the findings of Fischer & Dallmann (1991), the low-frequency mode can be viewed as an interaction between the zero-frequency and amplified travelling waves. Introducing a high-frequency harmonic disturbance results in a high-frequency oscillation in the upper part of the vortex. The high-frequency disturbances appear only once the cross-flow vortices have saturated and have considerably higher growth rates than the low-frequency secondary instability.

The results of the present investigation confirm that the high-frequency oscillations

found in the experiments of Deyhle & Bippes (1996), Kohama *et al.* (1991) and Lerche (1997) are a result of a secondary instability of the shear layer located on top of the cross-flow vortex, something also suggested by the results of Malik *et al.* (1994). This is the first time that this instability has been seen in direct numerical simulations. In particular it is interesting that both the low- and the high-frequency instability appeared as a result of a forcing by random noise. Thus both instabilities can be expected to exist in a real flow situation, and it is the nature of the disturbance environment in the flow of interest which determines which instability will appear. In a low noise environment one may expect the high-frequency instability to cause transition, since it has a so much higher growth rate, whereas in a flow with higher levels of free-stream turbulence transition may be caused by the low-frequency mode, since it has an onset further upstream. The latter scenario was found in an experiment of Müller & Bippes (1988) using a wind tunnel with rather high free-stream turbulence level. The dominant transition route may of course also be determined by the receptivity of the boundary layer to particular frequencies of disturbances in the free-stream turbulence.

For flows with low free-stream turbulence levels, the results of the present investigation indicate that the streamwise location of the start of transition should be well correlated with the neutral point of the high-frequency instability, since the turn-on of the instability is quite rapid and high values of the growth rate are reached quickly.

We wish to thank Anders Lundbladh whose initial calculations of these flows were used as a guide in the choice of numerical and physical parameter values. We also thank Ardeshir Hanifi for performing the PSE calculations using the DLR/FFA NOLOT/PSE code, and Stellan Berlin for all the help in checking the results.

This work has been performed at the Aeronautical Research Institute of Sweden (FFA) and has been supported by the Swedish National Board for Industrial and Technical Development (NUTEK).

REFERENCES

Bertolotti, F. P., Herbert, T. & Spalart, P. R. 1992 Linear and nonlinear stability of the Blasius boundary layer. *J. Fluid Mech.* **242**, 441–474.

Bippes, H. 1991 Experiments on transition in three-dimensional accelerated boundary-layer flows. *Proc. RAS Conf. on Boundary layer transition and control, Cambridge, England.*

Breuer, K. S. & Kuraishi, T. 1994 Transient growth in two- and three-dimensional boundary layers. *Phys. Fluids* **6**, 1983–1993.

Butler, K. M. & Farrell, B. F. 1992 Three-dimensional optimal perturbations in viscous shear flow. *Phys. Fluids* A **4**, 1637–1650.

Choudhari, M. 1994 Roughness induced generation of crossflow vortices in three-dimensional boundary layers. *Theor. Comput. Fluid Dyn.* **6**, 1–30.

Cooke, J. C. 1950 The boundary layer of a class of infinite yawed cylinders. *Proc. Camb. Phil. Soc.* **46**, 645–648.

Deyhle, H. & Bippes, H. 1996 Disturbance growth in an unstable three-dimensional boundary layer and its dependence on environmental conditions. *J. Fluid Mech.* **316**, 73–113.

Fischer, T. M. & Dallmann, U. 1991 Primary and secondary stability analysis of a three-dimensional boundary-layer flow. *Phys. Fluids* A **3**, 2378–2391.

Gregory, N., Stuart, J. T. & Walker, W. S. 1955 On the stability of three-dimensional boundary layers with application to the flow due to a rotating disk. *Phil. Trans. R. Soc. Lond.* A **248**, 155.

Hanifi, A., Henningson, D., Hein, S., Bertolotti, F. P. & Siemen, M. 1994 Linear nonlocal instability analysis – the linear NOLOT code. *FFA TN* 1994-54.

Henningson, D. S. 1995 Bypass transition and linear growth mechanisms. In *Advances in Turbulence V* (ed. R. Benzi), pp. 190–204. Kluwer.

Högberg, M. & Henningson, D. S. 1996 Cross-flow vortices and their secondary instability in Falkner-Skan-Cooke boundary layers. *FFA TN* 1996-60.

Kohama, Y., Saric, W. S. & Hoos, J. A. 1991 A high-frequency, secondary instability of crossflow vortices that leads to transition. *Proc. RAS Conf. on Boundary-Layer Transition and Control, Cambridge University, April 8–12.*

Lerche, T. 1997 Experimentelle Untersuchung nichtlinearen Strukturbildung im Transitionsprozeß einer instabilen Grenzschicht. *Fortscrittberichte, VDI, Reihe 7: Strömungstechnik*, Nr. 310.

Lingwood, R. J. 1995 Absolute instability of the boundary layer on a rotating disc. *J. Fluid Mech.* **299**, 17–33.

Lingwood, R. J. 1996 An experimental study of absolute instability of the rotating-disc boundary-layer flow. *J. Fluid Mech.* **314**, 373–405.

Lingwood, R. J. 1997 On the impulse response for swept boundary-layer flows. *J. Fluid Mech.* **344**, 317–334.

Lundbladh, A., Henningson, D. S. & Johansson, A. V. 1992 An efficient spectral integration method for the solution of the Navier–Stokes equations. *FFA TN* 1992-28.

Lundbladh, A., Schmid, P. J., Berlin, S. & Henningson, D. S. 1994 Simulation of bypass transition for spatially evolving disturbances. *AGARD-CP* 551, 18-1, 18-13.

Malik, M. R., Li, F. & Chang, C.-L. 1994 Crossflow disturbances in three-dimensional boundary layers: nonlinear development, wave interaction and secondary instability. *J. Fluid Mech.* **268**, 1–36.

Morkovin, M. V. 1969 On the many faces of transition. In *Viscous Drag Reduction* (ed. C. S. Wells), pp. 1–31. Plenum.

Morkovin, M. V. 1977 Instability, transition to turbulence and predictability. *AGARDograph* 236.

Müller, B., Bestek, H. & Fasel, H. 1993 Numerical simulation of the spatial disturbance development in transitional boundary layers along a swept plate. In *Near-Wall Turbulent Flows* (ed. R. M. C. So, C. G. Speziale & B. E. Launder). Elsevier.

Müller, B. & Bippes, H. 1988 Experimental study of instability modes in a three-dimensional boundary layer. *AGARD-CP* 438, No. 18.

Reed, H. L. & Saric, W. S. 1989 Stability of three-dimensional boundary layers. *Ann. Rev. Fluid Mech.* **21**, 235–284

Reddy, S. C. & Henningson, D. S. 1993 Energy growth in viscous channel flows. *J. Fluid Mech.* **252**, 209–238.

Schlichting, H. 1979 *Boundary-Layer Theory*, 7th Edn. McGraw-Hill.

Spalart, P. R., Crouch, J. D. & Ng, L. L. 1994 Numerical study of realistic perturbations in three-dimensional boundary layers. *AGARD-CP* 551, 30-1–30-10.

Trefethen, L. N., Trefethen, A. E., Reddy, S. C. & Driscoll, T. A. 1993 Hydrodynamic stability without eigenvalues. *Science* **261**, 578–584.

Wintergerste, T. & Kleiser, L. 1996 Direct numerical simulation of transition in a three-dimensional boundary layer. In *Transitional Boundary Layers in Aeronautics* (ed. R. W. A. M. Henkes & J. L. van Ingen), pp. 145–153. North Holland.